ACS APPLIED MATERIALS & INTERFACES

www.acsami.org

Research Article

Influence of the Rear Interface on Composition and Photoluminescence Yield of CZTSSe Absorbers: A Case for an Al_2O_3 Intermediate Layer

Antonio Cabas-Vidani,* Leo Choubrac, José A. Márquez, Thomas Unold, Matthias Maiberg, Roland Scheer, Hu Li, Klaus Leifer, Robin Pauer, Evgeniia Gilshtein, Ayodhya N. Tiwari, and Yaroslav E. Romanyuk

Cite This: *ACS Appl. Mater. Interfaces* 2021, 13, 19487−19496

Read Online

ACCESS | Metrics & More | Article Recommendations | Supporting Information

ABSTRACT: The rear interface of kesterite absorbers with Mo back contact represents one of the possible sources of nonradiative voltage losses ($\Delta V_{oc,nrad}$) because of the reported decomposition reactions, an uncontrolled growth of $MoSe_2$, or a nonoptimal electrical contact with high recombination. Several intermediate layers (IL), such as MoO_3, TiN, and ZnO, have been tested to mitigate these issues, and efficiency improvements have been reported. However, the introduction of IL also triggers other effects such as changes in alkali diffusion, altered morphology, and modifications in the absorber composition, all factors that can also influence $\Delta V_{oc,nrad}$. In this study, the different effects are decoupled by designing a special sample that directly compares four rear structures (SLG, SLG/Mo, SLG/Al_2O_3, and SLG/Mo/Al_2O_3) with a Na-doped kesterite absorber optimized for a device efficiency >10%. The IL of choice is Al_2O_3 because of its reported beneficial effect to reduce the surface recombination velocity at the rear interface of solar cell absorbers. Identical annealing conditions and alkali distribution in the kesterite absorber are preserved, as measured by time-of-flight secondary ion mass spectrometry and energy-dispersive X-ray spectroscopy. The lowest $\Delta V_{oc,nrad}$ of 290 mV is measured for kesterite grown on Mo, whereas the kesterite absorber on Al_2O_3 exhibits higher nonradiative losses up to 350 mV. The anticipated field-effect passivation from Al_2O_3 at the rear interface could not be observed for the kesterite absorbers prepared by the two-step process, further confirmed by an additional experiment with air annealing. Our results suggest that Mo with an in situ formed $MoSe_2$ remains a suitable back contact for high-efficiency kesterite devices.

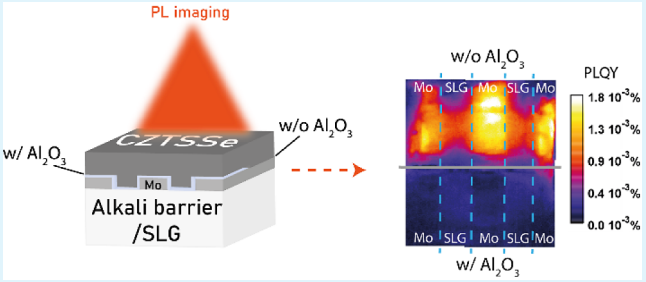

KEYWORDS: *kesterite, CZTSSe, solar cell, back contact, photoluminescence, Al_2O_3, nonradiative recombination*

Downloaded via 98.128.228.172 on June 4, 2021 at 12:38:56 (UTC).
See https://pubs.acs.org/sharingguidelines for options on how to legitimately share published articles.

1. INTRODUCTION

The best kesterite solar cell devices of many laboratories around the world[1−4] are approaching the world record efficiency of 12.6%, reached by IBM in 2013.[5] Despite all the efforts in finely optimizing the crystallization process, the problem of high $V_{oc,SQ}$ deficit (expressed as $V_{oc,SQ} - V_{oc}$, with $V_{oc,SQ}$ defined by the Shockley−Queisser limit) remains unresolved. The introduction of alkali metals proved to boost PV characteristics, but the minimum $V_{oc,SQ}$ deficit is still 0.29 V even for the best performing devices,[6,7] whereas for CIGS, it is below 0.15 V.[8]

Several studies suggest that the Mo back contact could be one of the factors limiting the V_{oc}. A possible reason is the decomposition of kesterite when in contact with the Mo layer at high temperatures.[9] Mo reacts with the chalcogen vapors forming a $Mo(S,Se)_2$ layer, the growth of which is difficult to control as it depends on multiple interrelated factors such as the Mo layer structure, duration, and temperature of the annealing process and chalcogen overpressure in the annealing chamber. Furthermore, it is still debated whether the $Mo(S,Se)_2$/CZTSSe interface ensures an appropriate electrical contact.[10]

The addition of an intermediate layer (IL) between the kesterite absorber and Mo has been reported to reduce or avoid the formation of $Mo(S,Se)_2$ by limiting the diffusion of Se to the back. Table 1 presents a collection of representative studies on the implementation of various materials as IL. While the influence on the $Mo(S,Se)_2$ growth varies, all papers report an increased efficiency relative to the baseline. So comes the

Received: February 4, 2021
Accepted: April 13, 2021
Published: April 19, 2021

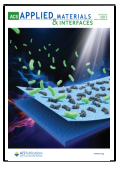

© 2021 The Authors. Published by American Chemical Society

Table 1. Comparison of Observed Influences (Change in $MoSe_2$ Thickness, Diffusion of Alkalis, and Other Additional Effects on Absorber Growth) Correlated with Introducing an IL between the Mo Layer and Kesterite Absorber from Recent Publications

IL material/absorber type	efficiency improvement (%)[a]	$Mo(S,Se)_2$ thickness	alkalis diffusion[b]	additional effects	reference
MoO_3 (10 nm)/CZTS	+19	-	↓Na ↑K	improved crystallization	12
MoO_3 (−)/CZTS	+30	↓	↑K	fewer voids at the back	13
TiN (200 nm)/CZTS(e)[c]	+100	↓	↑Na	improved crystallization	14
Al_2O_3 (3 nm)/CZTS	+10	↓	↑Na	ZnS segregation from back to the surface	15
TiB_2 (30 nm)/CZTS	+42	↓	-	smaller grains	16
ZnO (10 nm)/CZTSe	+140	-	-	bilayer formation + less secondary phases	17
a-SiC (10 nm)/CZTSe	+16	-	-	increased grain size	18

[a]Efficiency improvement relative to the baseline device presented in the reference. [b]An arrow pointing upward (downward) represents a measured increase (decrease) in the content of the indicated alkali metal in the kesterite absorber. [c]Both CZTS and CZTSe absorbers have been tested. The presence of TiN is beneficial in both cases. The results in the table are for the CZTS absorber only.

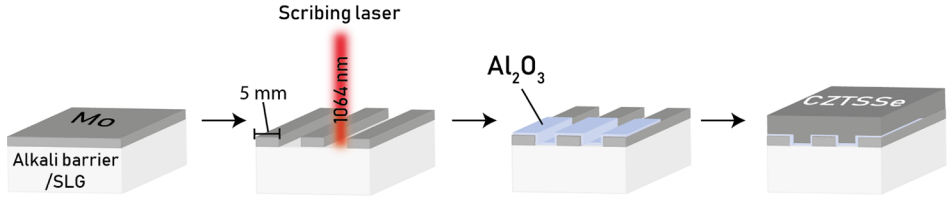

Figure 1. Process schematics to obtain the four rear structures (SLG/Mo, SLG/Mo/Al_2O_3, SLG, and SLG/Al_2O_3) with a single SLG substrate and a CZTSSe absorber.

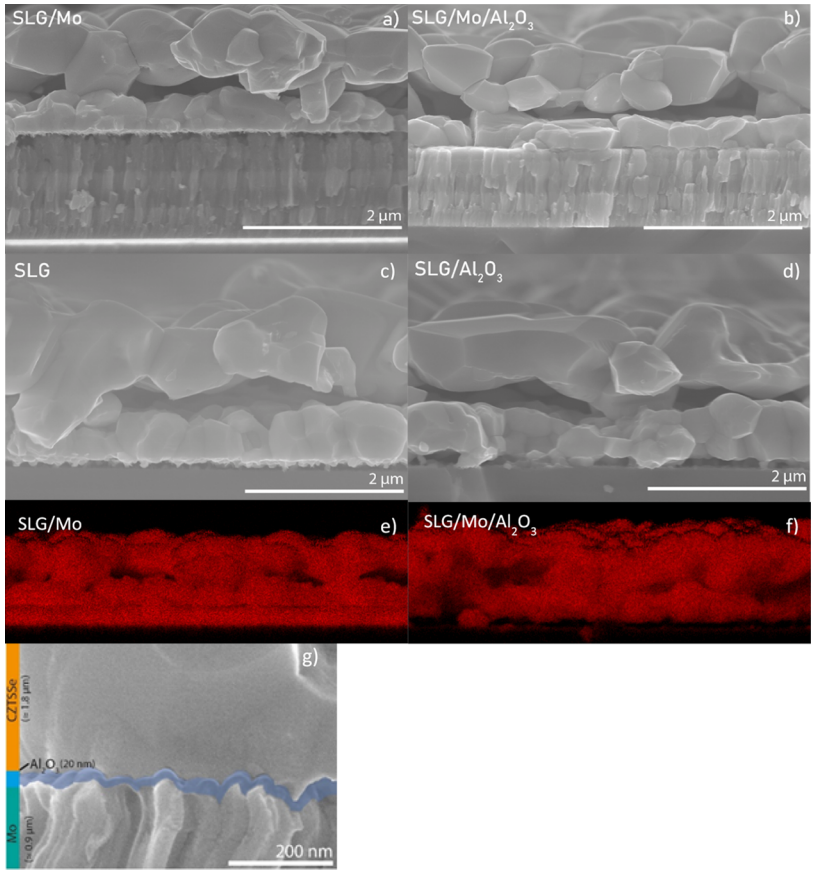

Figure 2. SEM cross-sectional images of the CZTSSe absorber on (a) SLG/Mo, (b) SLG/Mo/Al_2O_3, (c) bare SLG, and (d) SLG/Al_2O_3. (e), (f) SEM−EDS cross-sectional measurements for Se net counts for CZTSSe on SLG/Mo and SLG/Mo/Al_2O_3 structures, respectively. (g) High-resolution SEM cross section of the CZTSSe absorber deposited on Al_2O_3 on the Mo side. Al_2O_3 is highlighted with the blue color for clarity.

question: is the increase in performance related to the influence of the IL on the $Mo(S,Se)_2$ growth or on absorber growth dynamics? The question is justified by the additional reported effects (shown in Table 1) the IL has on alkali

https://doi.org/10.1021/acsami.1c02437
ACS Appl. Mater. Interfaces 2021, 13, 19487−19496

diffusion from the glass substrate, crystallization dynamics, and phase segregation. Further uncertainty is caused by Mo surface roughness. A conformal deposition is necessary to ensure barrier properties against Se diffusion.[11] These interconnected issues make it challenging to fully understand the origin of the performance improvement and if controlling $Mo(S,Se)_2$ thickness is beneficial.

In this study, a special sample design was considered to preserve the composition and annealing conditions of the absorber while allowing the comparison of four rear structures (Figure 1). The sample preparation can be divided into the following steps:

1 laser scribing of the Mo layer into 5 mm wide lines;
2 deposition of a conformal 20 nm thick Al_2O_3 layer by atomic layer deposition (ALD) on half of the scribed Mo layer and the other half was covered to keep it Al_2O_3 free;
3 spin-coating of a Na-doped CZTS precursor solution;
4 annealing in a rapid thermal processing (RTP) oven in a Se-rich atmosphere at temperatures up to 550 °C. We used the three-stage annealing profile process developed by Haass et al.,[19] with which a device efficiency of up to 11% can be achieved.

The as-obtained sample allows for a direct comparison of a single CZTSSe absorber grown on four rear structures: SLG/Mo, SLG/Mo/Al_2O_3, SLG, and SLG/Al_2O_3, corresponding to three different rear interfaces: Mo/CZTSSe, Al_2O_3/CZTSSe, and SLG/CZTSSe.

Al_2O_3 was the IL of choice because it reduces surface recombination and increases charge carrier lifetime, thanks to the low defect density at the interface.[20] The presence of fixed negative charges (corresponding to aluminum vacancies and/or oxygen interstitials) leads to upward band bending at the absorber interface, which repels the minority charge carriers.[21,22] This passivation effect is reported to be maximized after annealing treatments.[23,24]

Successful implementation of Al_2O_3 as a passivating layer has been reported for Si,[23,25] CIGS,[22,26−28] and CZTS[28−31] solar cell devices, but in such cases, the Al_2O_3 layer is typically patterned or thinner than 5 nm. This allows for carrier collection and absorber adhesion but limits the magnitude of the passivating effect.[23]

This study aims to clarify the influence of an IL at the rear interface on absorber growth and the V_{oc} of a single absorber. According to the literature,[23] the thickness of 20 nm of the Al_2O_3 layer and the annealing temperatures up to 550 °C should provide the best passivation properties. The effectiveness of the passivation is investigated by extracting the nonradiative recombination losses ($\Delta V_{oc,nrad}$) from quantitative photoluminescence (PL) measurements.

2. RESULTS AND DISCUSSION

2.1. Morphology and Crystallinity. Figure 2 presents the SEM cross sections of the absorber on the four rear structures (SLG/Mo, SLG/Mo/Al_2O_3, SLG, and SLG/Al_2O_3). There is no noticeable difference in morphology or thickness (about 1.7−2 μm) among the cross sections, indicating that the growth dynamics of the absorber layer was comparable. The bare Mo layer reached a thickness of about 1.3 μm after selenization due to $Mo(S,Se)_2$ formation. The Mo layer with Al_2O_3 on top measures about 0.9 μm (same as the as-deposited Mo layer), indicating that Al_2O_3 is an effective barrier for Se diffusion and that it withstands the annealing conditions. Figure 2g shows a high-resolution SEM cross section of the compact Al_2O_3 layer sandwiched between a CZTSSe grain and the Mo layer.

X-ray diffraction (XRD) measurements were carried out with a pinhole of 0.5 mm in diameter attached to the primary beam to assess whether the rear structure affects the absorber crystallinity. Such a configuration allows focusing the X-ray beam on specific locations of the sample. Figure 3a shows the full XRD pattern ($10° < 2\theta < 80°$) measured on four sample areas, each corresponding to a different rear structure. Bragg reflexes at 17.47°, 27.23°, and 45.25° confirm the CZTSSe phase.[32] $Mo(S,Se)_2$ diffraction peaks (31.76° and 56.32°) appear only for the side with bare Mo. Thus, $Mo(S,Se)_2$ is absent or too thin to be measured for the Mo/Al_2O_3 structure. This result is further confirmed through scanning electron

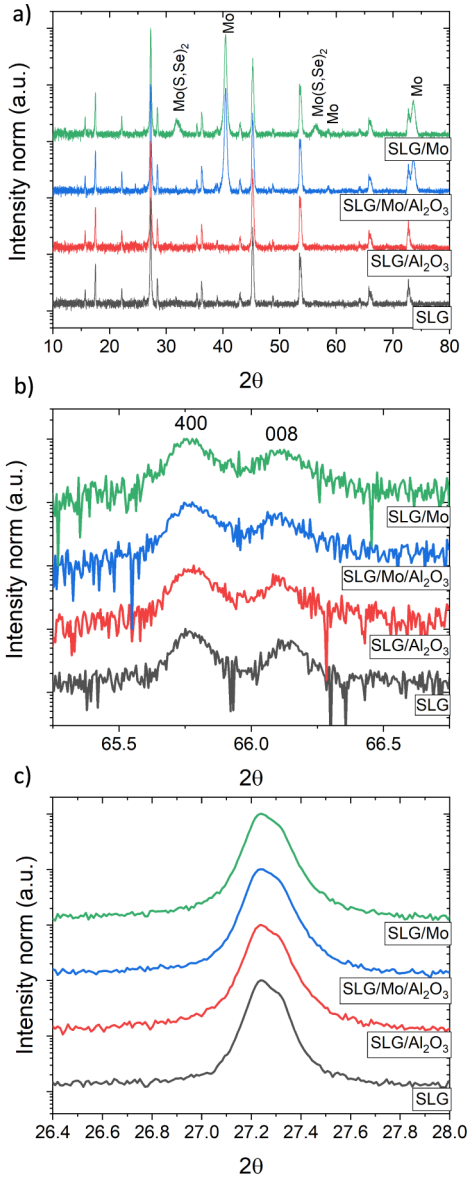

Figure 3. XRD patterns for the CZTSSe absorber grown on four different rear structures. (a) Full XRD pattern ($10° < 2\theta < 80°$). (b) High-resolution XRD pattern ($65° < 2\theta < 67°$) after stripping the Kα2 signal. (c) Zoomed 112 Bragg reflex.

https://doi.org/10.1021/acsami.1c02437
ACS Appl. Mater. Interfaces 2021, 13, 19487−19496

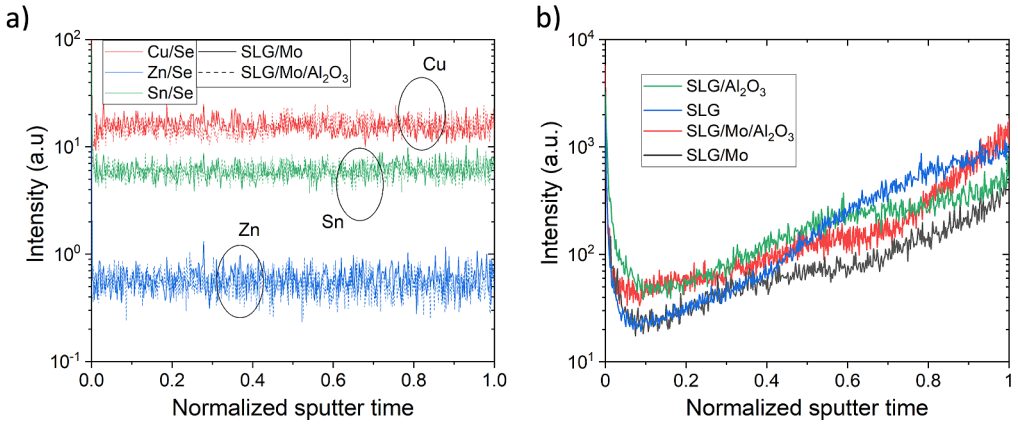

Figure 4. Normalized TOF-SIMS depth profiles of (a) Cu, Zn, and Sn for CZTSSe and SLG/Mo and SLG/Mo/Al_2O_3. (b) Comparison of normalized Na depth profiles for the CZTSSe absorber on the four structures SLG/Mo, SLG/Mo/Al_2O_3, SLG, and SLG/Al_2O_3.

microscopy and energy dispersive X-ray spectroscopy (SEM–EDS) Se maps of the cross sections for SLG/Mo/CZTSSe and SLG/Mo/Al_2O_3/CZTSSe structures (Figure 2e,f, respectively), where a Se-rich layer is visible beneath the CZTSSe absorber only for the SLG/Mo/CZTSSe structure. The 400-008 Bragg kesterite diffractions (Figure 3b), which represent lattice parameters *a* and *c*, respectively, are aligned among the four measurements, indicating a similar order/disorder of the Cu/Zn sublattice.[33,34] The primary 112 Bragg kesterite diffraction is positioned at 27.23° (Figure 3c) for each part of the absorber and indicates a S/(S + Se) ratio of about 5%, as calculated with Vegard's law.[35] Additional microprobe analysis of an absorber with a comparable composition measured a S content of 2.7 at. % and Se of 48.1 at.%, which corresponds to a S/(S + Se) ratio of 5%. The full width at half-maximum (FWHM) for the 112 diffraction peak among the three rear structures (SLG/Mo, SLG/Mo/Al_2O_3, and SLG/Al_2O_3) is 0.137 ± 0.003, whereas for bare glass, it is 0.127 ± 0.003. For other samples with the same composition, we measured the FWHM in the range of 0.194–0.247 and did not see any correlation with the rear structure. Therefore, the small difference measured for the sample in this manuscript is insignificant and within statistical error. Eventually, no secondary phases can be identified, although the presence of Zn(S,Se) and $Cu_2Sn(S,Se)_3$ impurity phases cannot be excluded since their Bragg reflexes coincide with those of CZTSSe and therefore cannot be distinguished by XRD.[36]

2.2. Composition. Time-of-flight secondary ion mass spectrometry (TOF-SIMS) allows investigating the elemental depth profiles qualitatively. In Figure 4, both the signal intensity of the matrix elements (Cu, Zn, and Sn) and the sputtering time are normalized, the first by the Se signal intensity and the latter by the absorber depth. The reported profile comparison between CZTSSe on SLG/Mo and SLG/Mo/Al_2O_3 structures is representative of all the measurements. The flat profiles of the matrix elements Cu, Zn, and Sn indicate that the presence or absence of Mo and/or Al_2O_3 does not influence the composition of the absorber throughout its thickness. The result is confirmed by EDS maps (Figure S5), where matrix elements (Cu, Zn, and Sn) are homogeneously distributed within the absorber thickness. The depth profile in Figure S4 for the CZTSSe absorber on the rear structure SLG/Mo/Al_2O_3 reveals the Al signal in the expected area between Mo and the absorber. One cannot rule out the presence of an unintentional Al doping in the CZTSSe absorber beyond the resolution of the SIMS measurement; however, small amounts of Al should not be harmful, but rather beneficial to electrical properties.[37] As indicated in Table 1, the addition of an IL can influence alkali-metal diffusion, with Na playing a significant role in affecting morphological and electrical characteristics of kesterite absorbers.[38−40] In this study, an SiO_x alkali barrier was sputtered before Mo deposition. This does not entirely block the Na out-diffusion from the SLG substrate but allows to control it. External Na doping is employed, in the form of NaCl added to the kesterite precursor solution, to provide a homogeneous Na source. A stronger Na signal at the absorber interfaces (Figure 4b) is expected and already observed in other studies. The signal peak at the front might be explained by Na evaporation from the SLG during the annealing and its subsequent condensation on the front surface of the absorber. In contrast, an increase in Na intensity toward the back of the absorber is due to Na diffusion from the SLG.[38,41,42] No systematic difference in the Na shape profile correlated with the rear structure can be observed. As measured by EDS, the Na concentration amounts to about 1 ± 0.4 at.% for each part of the sample (Figure S2d), thus confirming conclusions from TOF-SIMS measurements of a comparable Na concentration in the bulk of the absorber layer.

X-ray photoelectron spectroscopy (XPS) measurements were carried out to investigate chemical modifications of the surface (Figure S1). As observed in other studies, a thin oxide layer forms on the surface due to exposure to an ambient atmosphere, while the matrix elements exhibit similar depth profiles.[43]

A qualitative assessment of the metal ratios for the absorber bulk was obtained through X-ray fluorescence (XRF) mapping, which allows for detecting changes at a finer resolution than TOF-SIMS. In Figure 5, a correlation of Zn/Sn and Cu/Sn

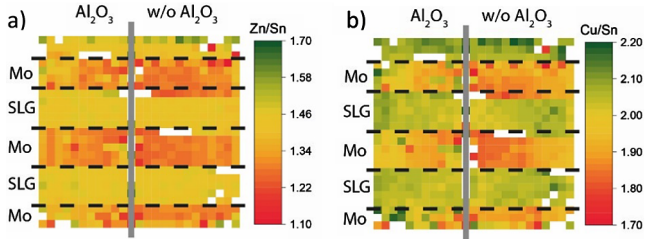

Figure 5. (a) Zn/Sn and (b) Cu/Sn XRF metal ratio maps.

https://doi.org/10.1021/acsami.1c02437
ACS Appl. Mater. Interfaces 2021, 13, 19487−19496

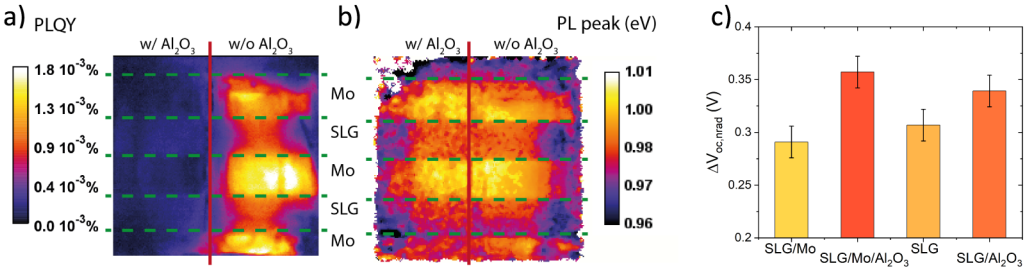

Figure 6. (a) Map of the PLQY. (b) Map of the PL peak position. (c) Conversion of PLQY intensity in nonradiative losses ($\Delta V_{oc,nrad}$).

metal ratios in the presence or absence of the Mo layer can be observed. In contrast, the presence of Al_2O_3 does not cause any noticeable influence on the composition. Areas without Mo have a Zn-richer and Sn-poorer composition compared to the areas with Mo. The heat reflection from metals like Mo can lead to lower temperatures during annealing than the areas without Mo, leading to increased reevaporation of Sn in the latter ones. The XRF fitting reliability was assessed by comparing the results with SEM−EDS measurements of a similarly processed sample (see Figure S2).

The material characterization presented so far demonstrates that the absorber growth was equivalent concerning morphology and the Na content comparable among the four sample areas corresponding to the four rear structures. Small variations in metal ratios were detected between Mo and Mo-free areas, whereas the ratios were identical for Al_2O_3- and Al_2O_3-free areas.

2.3. Nonradiative Recombination Losses ($\Delta V_{oc,nrad}$).

2.3.1. PL from the Front of the Absorber. Quantitative PL (also known as absolute PL or photoluminescence quantum yield, PLQY) allows calculating the nonradiative voltage losses following the formula $\Delta V_{oc,nrad} = -kT \ln(PLQY)$,[44] where PLQY is the measured calibrated PL intensity. The PLQY measurement was carried out with an excitation laser wavelength of 660 nm.

A color-coded PL image is presented in Figure 6a, where brighter areas imply a stronger PLQY intensity, thus reduced nonradiative voltage losses compared to the darker areas. Nonradiative voltage loss ($\Delta V_{oc,nrad}$) values are presented in Figure 6c. Figure 6b shows a color-coded map for the PL peak position, where color brightness is proportional to the PL peak.

Starting with the side without Al_2O_3 (right side of the sample in Figure 6a), one can compare CZTSSe grown on SLG and SLG/Mo. The kesterite grown on Mo has a brighter PLQY signal amounting to nonradiative voltage losses of about 290 mV, roughly 10−15 mV lower than on SLG. For reference, comparable losses were measured for Li-doped CZTSSe solar cell devices delivering an efficiency higher than 10%.[2] The PL peak position shifts comparably to the $\Delta V_{oc,nrad}$ difference between areas with or without Mo (Figure 6b). The PL emission of CZTSSe grown on Mo peaks at roughly 1 eV, about 10−15 meV higher than CZTSSe on areas without Mo. The peak shift agrees with the Sn content variation observed with XRF measurements in Figure 5, as similarly reported in previous studies.[45,46] By comparison, such a V_{oc} variation is within the experimental statistical error for the solution-processed kesterite in our laboratory.

However, the side with Al_2O_3 (left side of the sample) has the highest $\Delta V_{oc,nrad}$ losses of the sample, which amount to about 350 mV, regardless of the presence or absence of Mo beneath Al_2O_3. The result is surprising for two main reasons: the influence of the rear structures (SLG or SLG/Al_2O_3) and interface (Al_2O_3/CZTSSe) on the PL measured from the front should not be so pronounced for an absorber with a thickness of about 2 μm. Simulations of the PL intensity in function of the recombination velocity at the rear interface were carried out with a solar cell capacitance simulator (SCAPS) (see Figure 7) to evaluate the extent to which the rear interface can

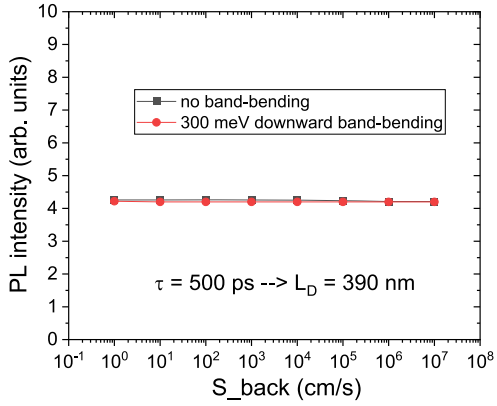

Figure 7. SCAPS simulation of the PL intensity in function of the recombination velocity at the back interface in the case of no band bending at the back and a downward band bending of 300 meV.

influence the PL measurement from the front surface. We used the following set of parameters to model the absorber: an absorber thickness of 2 μm, band gap of 1 eV, minority charge mobility μ = 120 cm^2/V,[47] and a lifetime τ = 500 ps,[48] which leads to a diffusion length of the minority charge carrier L_D < 0.5 μm based on the formula $L_D = (\tau\mu k_B T/q)^{0.5}$. Considering the surprising negative effect of the Al_2O_3 layer on PL, two hypothetical worst-case scenarios where the bands are not bending upward as expected were examined: one where Al_2O_3 does not create any band bending and the other with an arbitrary 300 meV downward band bending at the back. It can be observed that the PL intensity does not depend on the recombination velocity at the rear interface for both scenarios.

There is no measurable difference in composition and Na distribution between the CZTSSe absorber grown on Al_2O_3 (left side) and the one grown without (right side), which could justify the increased nonradiative losses. The result indicates that the presence of the Al_2O_3 IL must have additional effects that were not considered and cannot be assessed within the resolution of the absorber characterization techniques.

2.3.2. PL from the Back of the Absorber. The transparency of the SLG substrate allows carrying out PLQY measurements on the back of the sample on areas where Mo is not present. In

https://doi.org/10.1021/acsami.1c02437
ACS Appl. Mater. Interfaces 2021, 13, 19487−19496

this manner, the passivation of Al_2O_3 is directly assessed through the PL signal intensity. In this case, the analysis will be qualitative and the $\Delta V_{oc,nrad}$ will not be extracted since the system for the PLQY measurement is not calibrated for recording photon emissions through a layer of glass.

Figure 8 shows the PL map recorded from the back of the sample. It can be noticed that in this case, the intensity of the

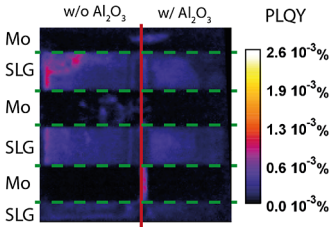

Figure 8. Map of the PLQY, as recorded through the SLG substrate.

PL between CZTSSe on SLG and SLG/Al_2O_3 rear structures is comparable. It follows that the presence of Al_2O_3 is not contributing to reducing the nonradiative recombination.

Considering the cross sections presented in Figure 1, one might suggest that the grainy morphology hinders the passivation or limits the absorption of the material. To rule out this factor, a Li-doped CZTSSe absorber displaying a compact morphology with large grains was considered (see Figure 3a for the cross section) and compared with the Na-doped absorber. The PL intensity measured from the back (Figure S3c) is of the same order of magnitude between the two samples. Thus, we can conclude that the morphological compactness did not influence the PL intensity or the contact quality with the Al_2O_3 layer.

2.4. Investigation of the Al_2O_3 Layer in an MOS Structure. To further understand the lacking passivation effect of the Al_2O_3, a metal-oxide semiconductor (MOS) structure, where the layer structure is SLG/Mo/CZTSSe/Al_2O_3 with e-beam evaporated Ni−Al contacts, was fabricated (schematic in Figure 9a). This type of device structure allows for a qualitative investigation of the CZTSSe/Al_2O_3 interface by capacitance−voltage (CV) measurements. Two MOS samples were prepared: one was measured after the Al_2O_3 deposition (AD = as deposited). The other was heated on a hot plate at 350 °C in air for 5 min after Al_2O_3 deposition (PDA = postdeposition annealing). The PDA is carried out at a temperature that is as close as possible to the annealing temperature used to crystallize CZTSSe absorbers,[49] so as to mimic its effect on the CZTSSe/Al_2O_3 interface, while avoiding absorber decomposition.[50,51]

For both devices, the capacitance was measured in forward and reverse bias in a voltage range of −2 to 2 V at 1 kHz (Figure 9b). Larger voltages caused the breakdown of the dielectric (Al_2O_3). The capacitance drops at a negative voltage for the AD device, indicating a negative flat band voltage. This correlates with the presence of net positive fixed charges in the Al_2O_3 layer; thus, the Al_2O_3 layer in the AD device is oxygen-deficient or aluminum-rich.[22] It would follow a downward band bending at the interface with the CZTSSe absorber, contrary to what is required for repelling the minority charge carriers. Kotipalli et al.[24] observed a similar behavior for the same type of device structure but with a CIGS absorber. The negative net fixed charges were recovered after an annealing procedure in a Se-rich atmosphere at $T > 500$ °C. At such a temperature, kesterite absorbers decompose;[52] thus, a similar annealing procedure was not considered for this study.

For the PDA device, no capacitance drop can be measured within the voltage range of the analysis. This entails that the fixed charges in the Al_2O_3 layer are neutralized or that their influence cannot be measured within the chosen voltage range. For a qualitative assessment of the charge profile, TOF-SIMS measurements were performed on the two MOS devices (Figure 9c). A significant influence can be observed for the oxygen profile throughout the Al_2O_3 layer depth. The PDA device presents a noticeably lower intensity for O^- ions, while

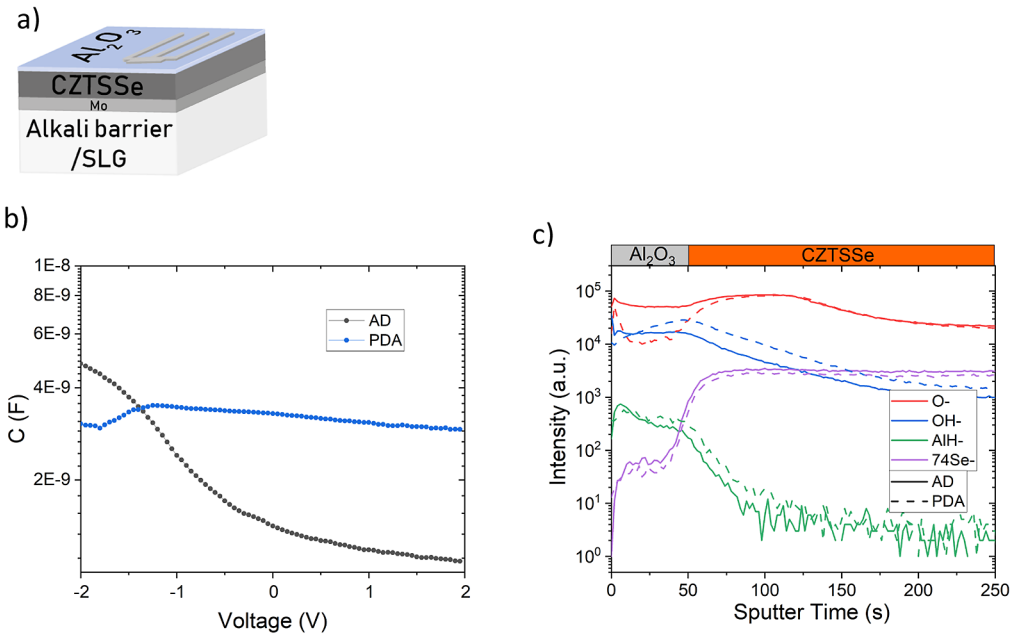

Figure 9. (a) Schematic of the MOS structure SLG/Mo/CZTSSe/Al_2O_3. (b) CV measurement at room-temperature of MOS devices with the Al_2O_3 as-deposited (AD) on Mo and after heating on a hotplate (PDA). (c) TOF-SIMS measurements of MOS devices for negative ions.

https://doi.org/10.1021/acsami.1c02437
ACS Appl. Mater. Interfaces 2021, 13, 19487−19496

the intensity for the OH^- ions increases correspondingly. This suggests hydrogen passivation of the dangling oxygen bonds, further reducing the amount of negative charges.[53] Therefore, we can conclude that high-temperature annealing changes Al_2O_3 composition, hence the amount of static charges, which shifts the flat band voltage to more negative values than −2 V. Eventually, this results in a lack of passivation at the CZTSSe interface, as is observed with the PL measurements in Figure 8.[21]

Our experiment was carried out on a kesterite absorber that was prepared with a two-stepmethod using a solution-processed precursor. There are many other methods for preparing the precursor including evaporation, sputtering, and spray-coating among others. As all of these approaches require a high-temperature crystallization step, we believe that our results are valid for kesterite absorbers obtained with the two-step method.[49] The effect, however, can also be dependent on the thickness of the Al_2O_3.

3. CONCLUSIONS

In this study, a single absorber was grown on four rear structures (SLG/Mo, SLG/Mo/Al_2O_3, SLG, and SLG/Al_2O_3), allowing the testing of the influence of the rear interfaces and presence of Mo on the absorber composition and nonradiative voltage losses, as extracted from the PLQY. Small variations in the composition could be observed between areas with or without the Mo layer, but not with the Al_2O_3 IL, while the Na distribution and quantity in the bulk and on the surface are comparable among all absorber parts.

From PL measurements on both the front and the back interfaces of the absorber, we observed the following:

For front PL: the part of the CZTSSe absorber with Al_2O_3 at the back has higher nonradiative losses than the part without it. The cause of the increased losses could not be identified with the resolution of the characterization techniques considered in the present study.

For back PL measured through the SLG substrate: the Al_2O_3 layer does not provide a measurable passivation effect. This can be explained by a net amount of positive fixed charges in the Al_2O_3 layer appearing after the kesterite precursor deposition.

Eventually, this study enabled us to verify that different rear structures can influence the absorber metal ratios, despite an unchanged morphology. While the IL Al_2O_3 limits the diffusion of Se to the back and avoids the contact of kesterite with the Mo layer, this does not lead to any positive impact on the $\Delta V_{oc,nrad}$ of an absorber optimized for a device efficiency >10%. This is explained by a negative influence of the two-step fabrication procedure necessary for kesterite absorbers on the passivating properties of the Al_2O_3 layer. The results further indicate that the Mo back contact represents the best solution for kesterite absorbers, and the reduction in $\Delta V_{oc,nrad}$ should be addressed by identifying and passivating the detrimental defects present in the kesterite bulk material.

4. EXPERIMENTAL SECTION

4.1. Chemicals. The precursor solution consisted of thiourea (99%+, Sigma-Aldrich), tin chloride dihydrate ($SnCl_2{\cdot}_2H_2O$, 98%, Sigma-Aldrich), zinc chloride ($ZnCl_2$, 99.99%, Alfa Aesar), copper chloride dihydrate ($CuCl_2{\cdot}2H_2O$, ≥99.99%, Sigma-Aldrich), and sodium chloride (NaCl, 99.99%, Alfa Aesar) dissolved in dimethyl sulfoxide (DMSO, 99.9%, Alfa Aesar).

4.2. Sample Preparation. A 200−300 nm thick SiO_x alkali diffusion barrier layer was sputtered onto a 1 mm thick soda-lime glass (SLG) with subsequent deposition of about 1 μm molybdenum. The molybdenum layer was patterned with a picosecond pulse laser with a wavelength of 1064 nm, power of 750 mW, and frequency of 20 kHz. The Al_2O_3 layer was deposited with a Fiji G2 ALD system (Veeco Instruments, Inc.). The process was performed at a substrate temperature of 150 °C with argon as a carrier gas at a base pressure of 25 Pa. The precursors were trimethylaluminum (TMA) (Sigma-Aldrich) and H_2O. TMA and H_2O were kept unheated. The growth rate was determined by ellipsometry on Si (100) reference substrates, and linear growth was observed with a growth rate of 0.99 Å·cycle^{-1}. The precursor solution was spin-coated onto the Mo layer and dried on a hotplate at 320 °C in air. The spin-coating and drying steps were repeated 12 times to obtain the desired precursor film thickness of about 1.7−2 μm. All samples were annealed in an RTP furnace (RTP Annealsys AS ONE 150) inside a closed graphite box with selenium pellets (800 mg). The temperature gradient employed for annealing was the three-stage process holding at 300, 500, and 550 °C.[19] After selenization, the absorbers were immersed for 5 min in a 10 wt % $(NH)_4S_2$ solution to clean the surface from contaminations and oxides.

4.3. Composition and Morphology. SEM measurements were performed using a Hitachi S-4800 electron microscope. EDS measurements were performed using a Zeiss 1550 SEM with the Oxford AZtec EDS system and an ESEM QuantaFEG650 from FEI (ThermoFisher) with detectors such as ETD (Everhart−Thornley detector) for SE imaging, CBS (concentric-backscattering detector) for BSE imaging, and EDX: ThermoNoran with SDD (Si-drift detector) 60 mm^2. XPS measurements were performed using a Quantum2000 photoelectron spectrometer from Physical Electronics with a monochromatic Al K_α source, operated at a base pressure below 10^{-9} mbar. XRF was performed with a Bruker M4 Tornado, using a rhodium tube operated at 20 keV as an X-ray source. A total of 625 data points (spot size ≈ 20μm diameter) were acquired over the sample. The spectra were then evaluated with an SLG/Mo/$MoSe_2$/CZTSSe multilayer model (using the Bruker software suite), using elemental metals and chalcogen layers as calibration standards. Depth profile measurements were performed with a TOF-SIMS system from ION-TOF using O^{+2} primary ions with 2 keV of ion energy, a current of 400 nA, and a raster size of 300 × 300 μm^2. An area of 100 × 100 μm^2 in-depth profiles was analyzed using Bi^+ ions with 25 keV of ion energy.

Microprobe analysis was carried out with a JXA-8530F JEOL SUPERPROBE, equipped with a field emission electron probe microanalyzer (FE-EPMA) and four crystal spectrometers (WDS) in a 3 × 3 mm^2 square area on the center of the absorber layer.

4.4. Crystallinity. XRD patterns for thin films were recorded in $2\theta/\theta$ scan mode using a Bruker D8 diffractometer with Cu Kα radiation (λ = 1.5418 Å, beam voltage: 40 kV, beam current: 40 mA, calibrated using Si(100) and Si(111) single crystals), a step size of 0.05°, and a scan rate of 0.5 s step^{-1} for the full pattern and a step size of 0.005° and a scan rate of 2 s step^{-1} for the high-resolution pattern. A pinhole of 0.5 mm in diameter was attached to the primary beam to limit the measurement area.

4.5. PL. The intensity calibrated PL data have been acquired with a custom setup described elsewhere.[54] The excitation has been carried out with 660 nm lasers coupled to homogenizer units. The excitation intensity was equivalent to >2 sun (6.1×10^{21} photons m^{-2} s^{-1}).[55] Relative PL measurements were carried out with a laser wavelength of 640 nm and an intensity equivalent to 1.22 W/cm^2.

4.6. MOS Device Characterization. Room-temperature CV measurements were carried out with an LCR meter from Agilent (E4990A) with an AC voltage of 30 mV at 25 °C.

■ ASSOCIATED CONTENT

Supporting Information

The Supporting Information is available free of charge at https://pubs.acs.org/doi/10.1021/acsami.1c02437.

XPS measurement of the absorber surface (Figure S1); comparison of the metal ratio values between XRF map

https://doi.org/10.1021/acsami.1c02437
ACS Appl. Mater. Interfaces 2021, 13, 19487−19496

and EDX measurements (Figure S2); SEM cross section and PL measurement of Li- and Na-doped absorbers deposited on SLG (Figure S3); TOF-SIMS depth profile for the CZTSSe absorber on the rear structure SLG/Mo/Al_2O_3 (Figure S4); and EDS maps for elements Cu, Zn, and Sn of CZTSSe absorbers (Figure S5) (PDF)

AUTHOR INFORMATION

Corresponding Author

Antonio Cabas-Vidani − *Laboratory for Thin Films and Photovoltaics, Empa-Swiss Federal Laboratories for Materials Science and Technology, Dübendorf 8600, Switzerland;* orcid.org/0000-0002-2692-5859; Email: antonio.cabasvidani@empa.ch

Authors

Leo Choubrac − *Department of Structure and Dynamics of Energy Materials, Helmholtz-Zentrum für Materialien und Energie GmbH, Berlin D-14109, Germany*

José A. Márquez − *Department of Structure and Dynamics of Energy Materials, Helmholtz-Zentrum für Materialien und Energie GmbH, Berlin D-14109, Germany;* orcid.org/0000-0002-8173-2566

Thomas Unold − *Department of Structure and Dynamics of Energy Materials, Helmholtz-Zentrum für Materialien und Energie GmbH, Berlin D-14109, Germany;* orcid.org/0000-0002-5750-0693

Matthias Maiberg − *Institute of Physics, Martin-Luther-University Halle-Wittenberg, Halle 06120, Germany*

Roland Scheer − *Institute of Physics, Martin-Luther-University Halle-Wittenberg, Halle 06120, Germany*

Hu Li − *Ångström Laboratory, Department of Engineering Sciences, Uppsala University, Uppsala 75121, Sweden; School of Microelectronics, Shandong University, Jinan 250100, China*

Klaus Leifer − *Ångström Laboratory, Department of Engineering Sciences, Uppsala University, Uppsala 75121, Sweden*

Robin Pauer − *Electron Microscopy Center, Empa-Swiss Federal Laboratories for Materials Science and Technology, Dübendorf 8600, Switzerland*

Evgeniia Gilshtein − *Laboratory for Thin Films and Photovoltaics, Empa-Swiss Federal Laboratories for Materials Science and Technology, Dübendorf 8600, Switzerland*

Ayodhya N. Tiwari − *Laboratory for Thin Films and Photovoltaics, Empa-Swiss Federal Laboratories for Materials Science and Technology, Dübendorf 8600, Switzerland*

Yaroslav E. Romanyuk − *Laboratory for Thin Films and Photovoltaics, Empa-Swiss Federal Laboratories for Materials Science and Technology, Dübendorf 8600, Switzerland*

Complete contact information is available at: https://pubs.acs.org/10.1021/acsami.1c02437

Author Contributions

The manuscript was written through the contributions of all authors. All authors have approved the final version of the manuscript.

Funding

H.L. and K.L. received funding from the Svenska Forskningsrådet Formas Foundation. H.L. received funding from the Qilu Young Scholar Program of Shandong University. A.C.-V., L.C., J.A.M., T.U., M.M., R.S., R.P., E.G., A.N.T., and Y.E.R. received funding from the Horizon2020 Framework Program.

Notes

The authors declare no competing financial interest.

ACKNOWLEDGMENTS

The Horizon2020 program supported this research under the project STARCELL (H2020-NMBP-03-2016-720907). The Formas Foundation (2019-01538) and the Qilu Young Scholar Program of Shandong University are also acknowledged for the financial support. The authors would also like to thank the whole team of the Laboratory for Thin Films and Photovoltaics.

REFERENCES

(1) Taskesen, T.; Neerken, J.; Schoneberg, J.; Pareek, D.; Steininger, V.; Parisi, J.; Gütay, L. Device Characteristics of an 11.4% CZTSe Solar Cell Fabricated from Sputtered Precursors. *Adv. Energy Mater.* **2018**, *8*, No. 1703295.

(2) Cabas-Vidani, A.; Haass, S. G.; Andres, C.; Caballero, R.; Figi, R.; Schreiner, C.; Márquez, J. A.; Hages, C.; Unold, T.; Bleiner, D.; Tiwari, A. N.; Romanyuk, Y. E. High-Efficiency $(Li_xCu_{1-x})_2ZnSn(S,Se)_4$ Kesterite Solar Cells with Lithium Alloying. *Adv. Energy Mater.* **2018**, *8*, No. 1801191.

(3) Son, D.-H.; Kim, S.-H.; Kim, S.-Y.; Kim, Y.-I.; Sim, J.-H.; Park, S.-N.; Jeon, D.-H.; Hwang, D.-K.; Sung, S.-J.; Kang, J.-K.; Yang, K.-J.; Kim, D.-H. Effect of solid-H_2S gas reactions on CZTSSe thin film growth and photovoltaic properties of a 12.62% efficiency device. *J. Mater. Chem. A* **2019**, *7*, 25279−25289.

(4) Giraldo, S.; Saucedo, E.; Neuschitzer, M.; Oliva, F.; Placidi, M.; Alcobé, X.; Izquierdo-Roca, V.; Kim, S.; Tampo, H.; Shibata, H.; Pérez-Rodríguez, A.; Pistor, P. How Small Amounts of Ge Modify the Formation Pathways and Crystallization of Kesterites. *Energy Environ. Sci.* **2018**, *11*, 582.

(5) Wang, W.; Winkler, M. T.; Gunawan, O.; Gokmen, T.; Todorov, T. K.; Zhu, Y.; Mitzi, D. B. Device Characteristics of CZTSSe Thin-Film Solar Cells with 12.6% Efficiency. *Adv. Energy Mater.* **2014**, *4*, 1−5.

(6) Gong, Y.; Zhang, Y.; Jedlicka, E.; Giridharagopal, R.; Clark, J. A.; Yan, W.; Niu, C.; Qiu, R.; Jiang, J.; Yu, S.; Wu, S.; Hillhouse, H. W.; Ginger, D. S.; Huang, W.; Xin, H. Sn^{4+} Precursor Enables 12.4% Efficient Kesterite Solar Cell from DMSO Solution with Open Circuit Voltage Deficit below 0.30 V. *Sci. China Mater.* **2020**, *64*, 1−9.

(7) Li, J.; Huang, Y.; Huang, J.; Liang, G.; Zhang, Y.; Rey, G.; Guo, F.; Su, Z.; Zhu, H.; Cai, L.; Sun, K.; Sun, Y.; Liu, F.; Chen, S.; Hao, X.; Mai, Y.; Green, M. A. Defect Control for 12. 5% Efficiency $Cu_2ZnSnSe_4$ Kesterite Thin-Film Solar Cells by Engineering of Local Chemical Environment. *Adv. Mater.* **2020**, *32*, No. 2005268.

(8) Krause, M.; Nikolaeva, A.; Maiberg, M.; Jackson, P.; Hariskos, D.; Witte, W.; Márquez, J. A.; Levcenko, S.; Unold, T.; Scheer, R.; Abou-Ras, D. Microscopic Origins of Performance Losses in Highly Efficient $Cu(In,Ga)Se_2$ Thin-Film Solar Cells. *Nat. Commun.* **2020**, *11*, No. 4189.

(9) Scragg, J. J.; Wätjen, J. T.; Edoff, M.; Ericson, T.; Kubart, T.; Platzer-Björkman, C. A Detrimental Reaction at the Molybdenum Back Contact in $Cu_2ZnSn(S,Se)_4$ Thin-Film Solar Cells. *J. Am. Chem. Soc.* **2012**, *134*, 19330−19333.

(10) Platzer-Björkman, C.; Barreau, N.; Bär, M.; Choubrac, L.; Grenet, L.; Heo, J.; Kubart, T.; Mittiga, A.; Sanchez, Y.; Scragg, J.; Sinha, S.; Valentini, M. Back and Front Contacts in Kesterite Solar Cells: State-of-the-Art and Open Questions. *J. Phys. Energy* **2019**, *1*, No. 044005.

(11) Englund, S.; Saini, N.; Platzer-Björkman, C. $Cu_2ZnSn(S,Se)_4$ from Annealing of Compound Co-Sputtered Precursors—Recent Results and Open Questions. *Sol. Energy* **2018**, *175*, 84−93.

(12) Park, J.; Huang, J.; Sun, K.; Ouyang, Z.; Liu, F.; Yan, C.; Sun, H.; Pu, A.; Green, M.; Hao, X. The Effect of Thermal Evaporated

MoO_3 Intermediate Layer as Primary Back Contact for Kesterite Cu_2ZnSnS_4 Solar Cells. *Thin Solid Films* **2018**, *648*, 39−45.
(13) Liu, L.; Lau, T.-K.; Zhi, Z.; Huang, L.; Wang, S.; Xiao, X. Modification of Mo Back Contact with MoO_{3-x} Layer and Its Effect to Enhance the Performance of Cu_2ZnSnS_4 Solar Cells. *Sol. RRL* **2018**, *2*, No. 1800243.
(14) Englund, S.; Grini, S.; Donzel-Gargand, O.; Paneta, V.; Kosyak, V.; Primetzhofer, D.; Scragg, J. J. S.; Platzer-Björkman, C. TiN Interlayers with Varied Thickness in $Cu_2ZnSnS(e)_4$ Thin Film Solar Cells: Effect on Na Diffusion, Back Contact Stability, and Performance. *Phys. Status Solidi A* **2018**, *215*, 1−11.
(15) Liu, F.; Huang, J.; Sun, K.; Yan, C.; Shen, Y.; Park, J.; Pu, A.; Zhou, F.; Liu, X.; Stride, J. A.; Green, M. A.; Hao, X. Beyond 8% Ultrathin Kesterite Cu_2ZnSnS_4 Solar Cells by Interface Reaction Route Controlling and Self-Organized Nanopattern at the Back Contact. *NPG Asia Mater.* **2017**, *9*, e401−e401.
(16) Liu, F.; Sun, K.; Li, W.; Yan, C.; Cui, H.; Jiang, L.; Hao, X.; Green, M. A. Enhancing the Cu_2ZnSnS_4 Solar Cell Efficiency by Back Contact Modification: Inserting a Thin TiB_2 Intermediate Layer at Cu_2ZnSnS_4/Mo Interface. *Appl. Phys. Lett.* **2014**, *104*, No. 051105.
(17) López-Marino, S.; Placidi, M.; Pérez-Tomás, A.; Llobet, J.; Izquierdo-Roca, V.; Fontané, X.; Fairbrother, A.; Espíndola-Rodríguez, M.; Sylla, D.; Pérez-Rodríguez, A.; Saucedo, E. Inhibiting the Absorber/Mo-Back Contact Decomposition Reaction in $Cu_2ZnSnSe_4$ Solar Cells: The Role of a ZnO Intermediate Nanolayer. *J. Mater. Chem. A* **2013**, *1*, 8338−8343.
(18) Colina, M.; Martin, I.; Giraldo, S.; Sanchez-Gonzalez, Y.; Kondrotas, R.; Oliva, F.; Izquierdo-Roca, V.; Perez-Rodriguez, A.; Coll, A.; Alcubilla, R.; Saucedo, E. Influence of Amorphous Silicon Carbide Intermediate Layer in the Back-Contact Structure of $Cu_2ZnSnSe_4$ Solar Cells. *IEEE J. Photovoltaics* **2016**, *6*, 1327−1332.
(19) Haass, S. G.; Diethelm, M.; Werner, M.; Bissig, B.; Romanyuk, Y. E.; Tiwari, A. N. 11.2% Efficient Solution Processed Kesterite Solar Cell with a Low Voltage Deficit. *Adv. Energy Mater.* **2015**, *5*, 1−7.
(20) Hsu, W. W.; Chen, J. Y.; Cheng, T. H.; Lu, S. C.; Ho, W. S.; Chen, Y. Y.; Chien, Y. J.; Liu, C. W. Surface Passivation of $Cu(In,Ga)Se_2$ Using Atomic Layer Deposited Al_2O_3. *Appl. Phys. Lett.* **2012**, *100*, 1−4.
(21) Weber, J. R.; Janotti, A.; Van De Walle, C. G. Native Defects in Al_2O_3 and Their Impact on III-V/Al_2O_3 Metal-Oxide-Semiconductor-Based Devices. *J. Appl. Phys.* **2011**, *109*, No. 033715.
(22) Joel, J. *Characterization of Al_2O_3 as CIGS Surface Passivation Layer in High-Efficiency CIGS Solar Cells*, Uppsala Universitet, 2014.
(23) Dingemans, G.; Seguin, R.; Engelhart, P.; Van De Sanden, M. C. M.; Kessels, W. M. M. Silicon Surface Passivation by Ultrathin Al_2O_3 Films Synthesized by Thermal and Plasma Atomic Layer Deposition. *Phys. Status Solidi RRL* **2010**, *4*, 10−12.
(24) Kotipalli, R.; Vermang, B.; Joel, J.; Rajkumar, R.; Edoff, M.; Flandre, D. Investigating the electronic properties of Al_2O_3/$Cu(In,Ga)Se_2$ interface. *AIP Adv.* **2015**, *5*, No. 107101.
(25) Dingemans, G.; Beyer, W.; Van De Sanden, M. C. M.; Kessels, W. M. M. Hydrogen Induced Passivation of Si Interfaces by Al_2O_3 Films and SiO_2/Al_2O_3 Stacks. *Appl. Phys. Lett.* **2010**, *97*, 2008−2011.
(26) Joel, J.; Vermang, B.; Larsen, J.; Donzel-Gargand, O.; Edoff, M. On the Assessment of CIGS Surface Passivation by Photoluminescence. *Phys. Status Solidi RRL* **2015**, *9*, 288−292.
(27) Keller, J.; Gustavsson, F.; Stolt, L.; Edoff, M.; Törndahl, T. On the Beneficial Effect of Al_2O_3 Front Contact Passivation in $Cu(In,Ga)Se_2$ Solar Cells. *Sol. Energy Mater. Sol. Cells* **2017**, *159*, 189−196.
(28) Bissig, B.; Guerra-Nunez, C.; Carron, R.; Nishiwaki, S.; La Mattina, F.; Pianezzi, F.; Losio, P. A.; Avancini, E.; Reinhard, P.; Haass, S. G.; Lingg, M.; Feurer, T.; Utke, I.; Buecheler, S.; Tiwari, A. N. Surface Passivation for Reliable Measurement of Bulk Electronic Properties of Heterojunction Devices. *Small* **2016**, *12*, 5339−5346.
(29) Cui, X.; Sun, K.; Huang, J.; Lee, C. Y.; Yan, C.; Sun, H.; Zhang, Y.; Liu, F.; Hossain, M. A.; Zakaria, Y.; Wong, L. H.; Green, M.; Hoex, B.; Hao, X. Enhanced Heterojunction Interface Quality to Achieve 9.3% Efficient Cd-Free Cu_2ZnSnS_4 Solar Cells Using Atomic Layer Deposition ZnSnO Buffer Layer. *Chem. Mater.* **2018**, *30*, 7860−7871.
(30) Park, J.; Huang, J.; Yun, J.; Liu, F.; Ouyang, Z.; Sun, H.; Yan, C.; Sun, K.; Kim, K.; Seidel, J.; Chen, S.; Green, M. A.; Hao, X. The Role of Hydrogen from ALD-Al_2O_3 in Kesterite Cu_2ZnSnS_4 Solar Cells: Grain Surface Passivation. *Adv. Energy Mater.* **2018**, *8*, 3−9.
(31) Lee, Y. S.; Gershon, T.; Todorov, T. K.; Wang, W.; Winkler, M. T.; Hopstaken, M.; Gunawan, O.; Kim, J. Atomic Layer Deposited Aluminum Oxide for Interface Passivation of $Cu_2ZnSn(S,Se)_4$ Thin-Film Solar Cells. *Adv. Energy Mater.* **2016**, *6*, 2−6.
(32) Nateprov, A.; Kravtsov, V. C.; Gurieva, G.; Schorr, S. Single Crystal X Ray Structure Investigation of Cu2ZnSnSe4. *Surf. Eng. Appl. Electrochem.* **2013**, *49*, 423−426.
(33) Choubrac, L.; Paris, M.; Lafond, A.; Guillot-Deudon, C.; Rocquefelte, X.; Jobic, S. Multinuclear (67Zn, 119Sn and 65Cu) NMR Spectroscopy—An Ideal Technique to Probe the Cationic Ordering in Cu_2ZnSnS_4 Photovoltaic Materials. *Phys. Chem. Chem. Phys.* **2013**, *15*, 10722−10725.
(34) Márquez, J.; Neuschitzer, M.; Dimitrievska, M.; Gunder, R.; Haass, S.; Werner, M.; Romanyuk, Y. E.; Schorr, S.; Pearsall, N. M.; Forbes, I. Systematic Compositional Changes and Their Influence on Lattice and Optoelectronic Properties of $Cu_2ZnSnSe_4$ Kesterite Solar Cells. *Sol. Energy Mater. Sol. Cells* **2016**, *144*, 579−585.
(35) Denton, A. R.; Ashcroft, N. W. Vegard's Law. *Phys. Rev. A* **1991**, *43*, 3161−3164.
(36) Dale, P. J.; Hoenes, K.; Scragg, J.; Siebentritt, S. A. Review of the Challenges Facing Kesterite Based Thin Film Solar Cells. *Conf. Rec. IEEE Photovoltaic Spec. Conf.* **2009**, 002080−002085.
(37) Kuo, D. H.; Tsega, M. Hole Mobility Enhancement of Cu-Deficient $Cu_{1.75}Zn(Sn_{1-x}Al_x)Se_4$ Bulks. *J. Solid State Chem.* **2013**, *206*, 134−138.
(38) Abzieher, T.; Schnabel, T.; Hetterich, M.; Powalla, M.; Ahlswede, E.; Kesterite, I. Source and Effects of Sodium in Solution-Processed Kesterite Solar Cells. *Phys. Status Solidi A* **2016**, *213*, 1039−1049.
(39) Gershon, T.; Shin, B.; Bojarczuk, N.; Hopstaken, M.; Mitzi, D. B.; Guha, S. The Role of Sodium as a Surfactant and Suppressor of Non-Radiative Recombination at Internal Surfaces in Cu_2ZnSnS_4. *Adv. Energy Mater.* **2015**, *5*, 1−8.
(40) Sutter-Fella, C. M.; Stückelberger, J. A.; Hagendorfer, H.; La Mattina, F.; Kranz, L.; Nishiwaki, S.; Uhl, A. R.; Romanyuk, Y. E.; Tiwari, A. N. Sodium Assisted Sintering of Chalcogenides and Its Application to Solution Processed $Cu_2ZnSn(S,Se)_4$ Thin Film Solar Cells. *Chem. Mater.* **2014**, *26*, 1420−1425.
(41) Grini, S.; Sopiha, K. V.; Ross, N.; Liu, X.; Bjørheim, T. S.; Platzer-Björkman, C.; Persson, C.; Vines, L. Strong Interplay between Sodium and Oxygen in Kesterite Absorbers: Complex Formation, Incorporation, and Tailoring Depth Distributions. *Adv. Energy Mater.* **2019**, *9*, 1−9.
(42) Haight, R.; Shao, X.; Wang, W.; Mitzi, D. B. Electronic and elemental properties of the Cu_2 $ZnSn(S,Se)_4$ surface and grain boundaries. *Appl. Phys. Lett.* **2014**, *104*, No. 033902-1.
(43) Andres, C.; Schwarz, T.; Haass, S. G.; Weiss, T. P.; Carron, R.; Caballero, R.; Figi, R.; Schreiner, C.; Bürki, M.; Tiwari, A. N.; Romanyuk, Y. E. Decoupling of Optoelectronic Properties from Morphological Changes in Sodium Treated Kesterite Thin Film Solar Cells. *Sol. Energy* **2018**, *175*, 94−100.
(44) Redinger, A.; Kretzschmar, S.; Unold, T. Quantitative PL Imaging of Thin Film Solar Cells—Potential and Pitfalls. *2017 IEEE 44th Photovoltaic Specialists Conference PVSC* **2017**, 1−4.
(45) Azzouzi, M.; Cabas-Vidani, A.; Haass, S. G.; Röhr, J. A.; Romanyuk, Y. E.; Tiwari, A. N.; Nelson, J. Analysis of the Voltage Losses in CZTSSe Solar Cells of Varying Sn Content. *J. Phys. Chem. Lett.* **2019**, *10*, 2829−2835.
(46) Larramona, G.; Levcenko, S.; Bourdais, S.; Jacob, A.; Choné, C.; Delatouche, B.; Moisan, C.; Just, J.; Unold, T.; Dennler, G. Fine-Tuning the Sn Content in CZTSSe Thin Films to Achieve 10.8% Solar Cell Efficiency from Spray-Deposited Water-Ethanol-Based Colloidal Inks. *Adv. Energy Mater.* **2015**, *5*, 1−10.

https://doi.org/10.1021/acsami.1c02437
ACS Appl. Mater. Interfaces 2021, 13, 19487−19496

(47) Hempel, H.; Hages, C. J.; Eichberger, R.; Repins, I.; Unold, T. Minority and Majority Charge Carrier Mobility in $Cu_2ZnSnSe_4$ revealed by Terahertz Spectroscopy. *Sci. Rep.* **2018**, *8*, 1−9.
(48) Hages, C. J.; Redinger, A.; Levcenko, S.; Hempel, H.; Koeper, M. J.; Agrawal, R.; Greiner, D.; Kaufmann, C. A.; Unold, T. Identifying the Real Minority Carrier Lifetime in Nonideal Semiconductors: A Case Study of Kesterite Materials. *Adv. Energy Mater.* **2017**, *7*, No. 1700167.
(49) Ratz, T.; Brammertz, G.; Caballero, R.; León, M.; Canulescu, S.; Schou, J.; Gütay, L.; Pareek, D.; Taskesen, T.; Kim, D.-H.; Kang, J.-K.; Malerba, C.; Redinger, A.; Saucedo, E.; Shin, B.; Tampo, H.; Timmo, K.; Nguyen, N. D.; Vermang, B. Physical Routes for the Synthesis of Kesterite. *J. Phys. Energy* **2019**, *1*, No. 042003.
(50) Scragg, J. J.; Ericson, T.; Kubart, T.; Edoff, M.; Platzer-Björkman, C. Chemical Insights into the Instability of Cu_2ZnSnS_4 Films during Annealing. *Chem. Mater.* **2011**, *23*, 4625−4633.
(51) Redinger, A.; Berg, D. M.; Dale, P. J.; Siebentritt, S. The Consequences of Kesterite Equilibria for Efficient Solar Cells. *J. Am. Chem. Soc.* **2011**, *133*, 3320−3323.
(52) Clark, J. A.; Uhl, A. R.; Martin, T. R.; Hillhouse, H. W. Evolution of Morphology and Composition during Annealing and Selenization in Solution-Processed $Cu_2ZnSn(S,Se)_4$. *Chem. Mater.* **2017**, *29*, 9328−9339.
(53) Shin, B.; Weber, J. R.; Long, R. D.; Hurley, P. K.; Van De Walle, C. G.; McIntyre, P. C. Origin and Passivation of Fixed Charge in Atomic Layer Deposited Aluminum Oxide Gate Insulators on Chemically Treated InGaAs Substrates. *Appl. Phys. Lett.* **2010**, *96*, 1−4.
(54) Redinger, A.; Levcenko, S.; Hages, C. J.; Greiner, D.; Kaufmann, C. A.; Unold, T. Time Resolved Photoluminescence on $Cu(In, Ga)Se_2$ absorbers: Distinguishing Degradation and Trap States. *Appl. Phys. Lett.* **2017**, *110*, No. 122104.
(55) Kirchartz, T.; Márquez, J. A.; Stolterfoht, M.; Unold, T. Photoluminescence-Based Characterization of Halide Perovskites for Photovoltaics. *Adv. Energy Mater.* **2020**, *10*, No. 1904134.

https://doi.org/10.1021/acsami.1c02437
ACS Appl. Mater. Interfaces 2021, 13, 19487−19496